

Article

Nondestructive Evaluation of Strain-Induced Phase Transformation and Damage Accumulation in Austenitic Stainless Steel Subjected to Cyclic Loading

Chungseok Kim

Department of Materials Science and Engineering, Chosun University, Gwangju 501-759, Korea; chs2865@chosun.ac.kr

Received: 24 October 2017; Accepted: 27 December 2017; Published: 29 December 2017

Abstract: Strain-induced phase transformation and damage accumulation in austenitic stainless steel subjected to cyclic loading were investigated by nondestructive evaluation. The cyclic loading test was performed at various strain amplitudes at the same strain rate. The volume fraction of the strain-induced phase transformation (α' -martensite) was determined by ferrite scope and magnetic coercivity measurement. The damage accumulation and microstructure of cyclic loading specimens were characterized by microstructural observation. The cyclic hardening and cyclic softening behavior are discussed in terms of the generation of strain-induced martensite phases and a dislocation substructure at each strain amplitude. The volume fraction of the strain-induced phase increased with the strain amplitude. The increase in α' -martensite was evaluated by measuring the ultrasonic nonlinearity parameter. The presence of α' -martensite is sufficient to distort the austenitic matrix due to an interface misfit between the austenite matrix and α' -martensite, resulting in wave distortion of the longitudinal wave. From this wave distortion, super-harmonics may be generated with nucleation of the strain-induced martensite, a process that strongly depends on the strain amplitude.

Keywords: low-cycle fatigue; strain-induced martensite; non-destructive evaluation; ultrasonic nonlinearity

1. Introduction

Austenitic AISI 316L stainless steels are widely used as structural components in heavy industry facilities due to their good corrosion resistance, weldability, and mechanical properties [1–3]. These structural components are usually subjected to severe cyclic mechanical stress. Therefore, due to its importance in the makeup of large industrial parts, there is a growing interest in the failure of austenitic stainless steel. This particular subject is important insofar as a significant percentage of the failures that occur in high-temperature equipment utilizing stainless steels result from the presence of cyclic stresses. “Cyclic fatigue” refers to the weakening of materials caused by the repeated application of external loads or by the progressive and localized structural damage that occurs when materials are subjected to cyclic loading [4,5].

In particular, metastable austenitic stainless steels undergo strain-induced martensitic transformation (α' -martensite), in which the metastable austenite phase is transformed into the thermodynamically more stable α' -martensite phase due to plastic deformation [6,7]. This strain-induced martensitic transformation enhances the work hardening of metastable austenitic stainless steels. However, structural components designed for severe high-temperature and high-pressure environments at the power and chemical plant facilities deteriorate during their operation, leading to growing safety and integrity concerns. Therefore, a safety evaluation and a life assessment of such structures are important and highly necessary. The fatigue behavior of this steel must be investigated and monitored to ensure both its structural safety and reliable operation.

A fatigue damage evaluation with a nondestructive technique matters increasingly for the safe and reliable performance of structural and mechanical components. During service, mechanical or thermal overloading can occur, leading to components sometimes becoming locally damaged. During further operation, the damaged component may then fail to follow the predicted fatigue behavior; its lifetime is shortened. Consequently, the risk of early failure must be considered. Therefore, as part of the in-service inspection process, it is relevant to detect the locations and regions of early damage. However, to quantify the state of the damage with a nondestructive evaluation (NDE) technique represents a significant challenge [8].

Austenitic AISI 316L steel is non-ferromagnetic and metastable. Under high-stress or high-strain conditions, some of the austenite phases are known to transform into ferromagnetic α' -martensite, a strain-induced type of martensite [9,10]. This strain-induced martensite is in the ferromagnetic phase. The magnetic properties of materials are very sensitive to microstructural changes in the materials, and indeed, magnetic methods have been used to estimate microstructural changes affecting phase transformation, crystalline grains, and particle size that occur in various steels [11–13]. The use of nonlinear ultrasonic methods can also promote an understanding of the evolution and accumulation of the plastic deformation of materials occurring in the very early stages of fatigue [14–17]. An enhanced generation of high-order harmonics resulting from the distortion of ultrasonic waves propagated through the materials has been demonstrated by various authors, and recent experimental studies and physical models provide strong evidence that the ultrasonic nonlinearity parameter (β) is highly dependent on fatigue degradation [18,19].

The purpose of this study is to investigate low-cycle fatigue damage of AISI 316L stainless steels using a magnetic and acoustic evaluation. For this purpose, a nonlinear ultrasonic measurement is performed in austenitic stainless steels. We apply the oblique incidence technique in order to obtain the ultrasonic nonlinearity parameter. Additionally, we measure the magnetic characteristics in order to determine the microstructural evolution of the material. We then make a number of metallurgical observations on fatigue failure at various strain amplitudes. Following this, we attempt to determine the effects of microstructures on both the generation of high-order harmonics of the ultrasonic wave and on the variation in the magnetic properties during low-cycle fatigue in austenitic AISI 316L stainless steels, by correlating the results of NDE measurements with microstructural evolution.

2. Materials and Methods

The nominal chemical composition of AISI 316L austenitic stainless steel used in this investigation is C: 0.002, Mo: 2.47, Ni: 10.82, Cr: 17.41 wt. %, and Fe: balance. The low-cycle fatigue (LCF) test was performed in accordance with the procedure defined in the American Society for Testing and Materials (ASTM) standard E606-92 [20] using a computer-controlled servo-hydraulic testing machine. A plate-type specimen with a gauge length of 15 mm and thickness of 10 mm was used for the LCF test under fully reversed total strain amplitude control in the air. The strain amplitude varied from 0.5% to 1.7%, and the strain rate was 3×10^{-3} /s.

Microstructural analyses were performed on samples prepared by mechanical polishing and vibration polishing followed by chemical etching. The surface microstructure was observed by optical microscopy (OM). To observe the dislocation substructures by transmission electron microscopy (TEM), thin foils were prepared by twin jet polishing in a solution made of 25% of perchloric acid. The magnetic phases such as delta ferrite and strain-induced martensite present in austenitic steel after fatigue damage were measured using a ferrite scope (PMP30). Additionally, a magnetic force microscope (MFM) was used to reconstruct the magnetic structures of the sample surface, including the domain walls (Bloch and Neel), closure domains, recorded magnetic bits, as well as other features.

To monitor the ferromagnetic α' -martensite transformation during fatigue deformation, the magnetic parameters were determined for all fatigue-failed specimens. The magnetic parameters, comprised of coercivity, remanence, and saturation magnetization, were determined from the magnetic hysteresis curve obtained with a vibrating sample magnetometer (VSM).

To avoid any inherent harmonic distortion from the transducer, the transmitting piezoelectric transducer must be driven at a low voltage. However, the input voltage for the transmitter must not be too low when attempting to observe the high-order harmonics. A high-power gate amplifier (Ritec, RAM5000 SNAP) was therefore used to provide high-power tone-burst signals to the transmitter. A schematic diagram of the experimental setup used to measure the acoustic nonlinearity of an oblique incidence measurement technique is shown in Figure 1. The oblique incidence technique has a practical utility for the structural facilities of mechanical plants due to how easily accessible the structure surfaces under investigation are [21]. The amplified high-voltage signal passes through a 6-dB attenuator (RA-31) to decrease the driving voltage to less than 60 V_{pp} and 50 Ω termination, which impedes a transient electric current from the mismatch of electrical impedance between the amplifier and the piezoelectric transducer. In the oblique incidence measurement technique, the transmitting transducer and the receiving transducer are placed on the same side of the specimen. The transmitting and receiving transducers were attached via a 45-degree refractive angle wedge. Additionally, one skip distance was measured as 22 mm.

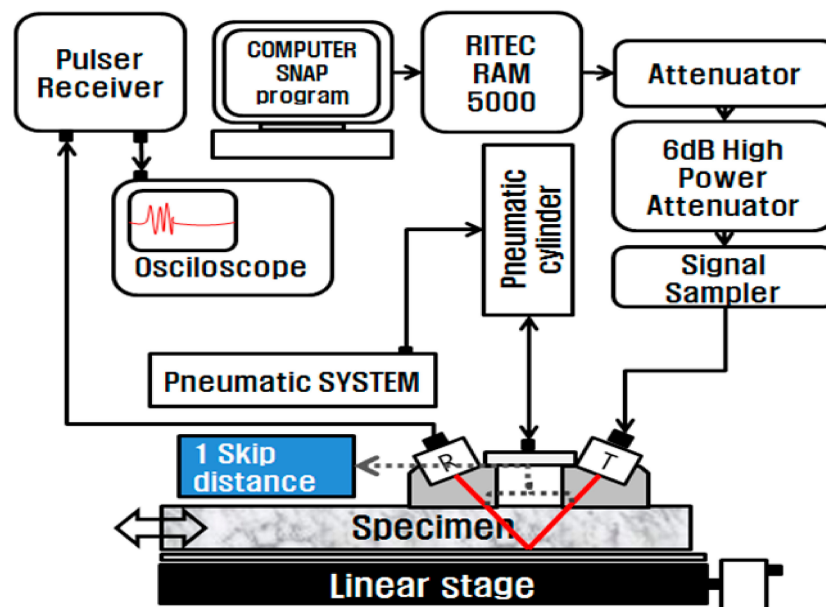


Figure 1. Schematic diagram of the experimental setup for measuring acoustic nonlinearity via the oblique incidence technique.

The received signal was digitally processed using fast Fourier transform (FFT) power spectral analysis to obtain the amplitudes of the fundamental and second-order harmonic frequencies.

If we assume that the attenuation can be neglected, then the motion equation for a longitudinal wave in a solid, using the generalization of Newton's law, may be written as [22,23]:

$$\rho \frac{\partial^2 u_i}{\partial t^2} = \frac{\partial \sigma_{ij}}{\partial X_j} \quad (1)$$

where t is time, ρ is the mass density of the solid, u_i and X_i are the components of the displacement and the position vectors, and σ_{ij} is the stress tensor.

If we consider the one-dimensional wave propagation of a pure longitudinal wave in an isotropic solid material, we obtain [14]:

$$\frac{\partial^2 u_1}{\partial t^2} = c^2 \left(1 + \beta \frac{\partial u_1}{\partial X_1} \right) \frac{\partial^2 u_1}{\partial X_1^2} \quad (2)$$

where $c = \sqrt{(E/\rho)}$ is the longitudinal wave velocity, and β is the nonlinearity parameter.

An approximate solution of Equation (2) is $u = u_0 + u_1$, where $u_0 = A_1 \sin(kX - \omega t)$ at the boundary condition and $X = 0$; the solution u_1 can then be obtained via an iterative process [14]:

$$u(X, t) = A_1 \sin(kX - \omega t) - \frac{A_1^2 k^2 \beta X}{8c^2} \cos 2(kX - \omega t) \quad (3)$$

where A_1 is the particle displacement amplitude of the fundamental wave. For the second harmonic wave, A_2 is $(\beta A_1^2 k^2 X)/8c^2$, k is the propagation constant $2\pi/\lambda$ with λ defined as the wavelength, and $\omega = 2\pi f$ with f defined as the frequency. Equation (3) indicates that the ultrasonic nonlinearity parameter may be obtained from measurements of the absolute amplitudes of the fundamental acoustic wave and second harmonic wave. Therefore, nonlinearity parameter β is determined as follows:

$$\beta = \frac{8c^2 A_2}{A_1^2 k^2 X} \quad (4)$$

The amplitude of the fundamental wave (A_1) and second harmonic wave (A_2) can be measured from the fast Fourier transform (FFT) of the signal fed to the oscilloscope channel; the nonlinear ultrasonic parameter (β) is then measured using the proportional relationship, $\beta \propto A_2/A_1^2$, which is the relative nonlinear parameter value.

3. Results and Discussion

Figure 2 shows the low-cycle fatigue properties of austenitic AISI 316L stainless steels. Cyclic stress response curves showing the relationship between the stress amplitude and the number of cycles at five different total strain amplitudes are shown in Figure 1a. The number of fatigue cycles to failure decreased with an increasing strain amplitude. This allowed an examination of the variation in the maximum load with the number of cycles, which could indicate whether the material cyclically hardened, softened, or was stable.

Cyclic hardening was observed in the initial cycles within several tens of cycles; this was followed by slight second hardening at strain amplitudes ranging from 0.8% to 1.1%, and slight softening following the initial hardening was observed at a strain amplitude of 0.5%. At strain amplitudes greater than 1.1%, the material exhibited strain hardening without reaching its saturated value until the final fracture. The initial hardening and subsequent second hardening are believed to result, respectively, from the increased dislocation density and from the α' -martensite transformation. The specimens were subjected to fully reversed cyclic loading under strain control. The number of stress reversals to failure was monitored and derived from the resulting strain-life plot, shown in Figure 2. The constants in the Manson-Coffin equation were derived by performing linear regression on the elastic and plastic lines. To determine the Basquin and Coffin-Manson parameters, the number of fatigue cycles to failure (N_f) is presented as a function of the total plastic and elastic strain amplitudes [24]. The Basquin and Coffin-Manson parameters are summarized in Table 1. These Coffin-Manson parameters are consistent with previous reports [25].

Table 1. Summary of the determined Coffin-Manson parameters.

Fatigue Strength Coefficient (σ'_f)	Fatigue Strength Exponent (b)
1392 MPa	−0.16
Fatigue Ductility Coefficient (ϵ'_f)	Fatigue Ductility Exponent (c)
0.23	−0.47

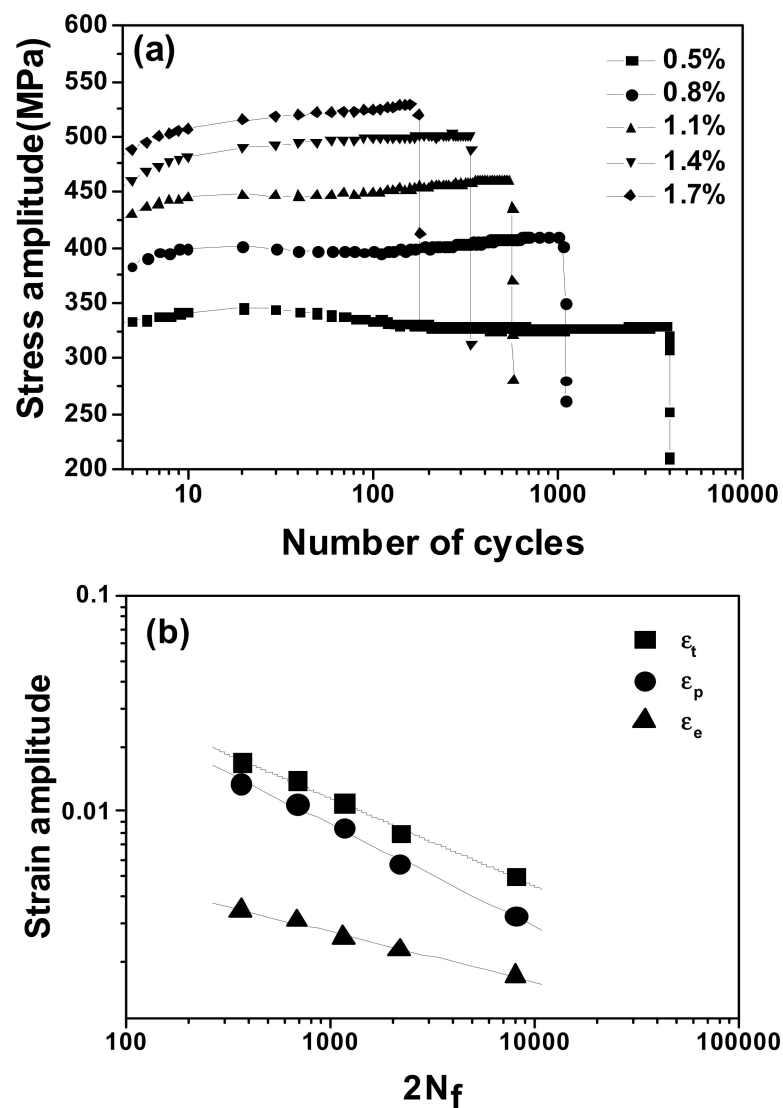


Figure 2. Low-cycle fatigue behavior of austenitic 316 stainless steel: (a) cyclic stress response curves under various strain amplitudes and (b) Basquin and Coffin-Manson plot. Cyclic hardening was observed in the initial cycles within several tens of cycles and was followed by slight second hardening.

The optical microstructures of the AISI 316L stainless steel after fatigue failure under various strain amplitudes are shown in Figure 3, and they are compared with the microstructure of the as-received specimen. The as-received specimen consisted of a single austenite phase, whereas the austenite and α' martensite phases were observed in all fatigue-failed specimens; the α' -martensite phase is denoted by arrows near the grain boundaries. The α' -martensite phases observed in the fatigue-failed AISI 316L stainless steel were induced by fatigue strain. The amount of α' -martensite increases with increasing strain amplitude in these optical micrographs and develops near grain boundaries and near the inter-regions of slips.

Figure 4 shows transmission electron micrographs of the dislocation substructure both in the as-received specimen and after fatigue failure at a strain amplitude of 1.7%. The typical dislocation cell microstructure was well-developed. The initial cyclic hardening was attributed to the increased dislocation density, and the subsequent softening was ascribed to the formation of dislocation cells resulting from fatigue. To investigate the transportation of the martensite phase in the AISI 316 steel specimen, we conducted X-ray diffraction (XRD) tests. The XRD profiles of the fatigue-failed specimens under various strain amplitudes are shown in Figure 5. The diffraction peak of $2\theta = 44.5$ is identified

in the as-received sample as delta ferrite. The intensity of this peak increased with a higher strain amplitude, as indexed with $\delta + \alpha'$. This increase in XRD intensity was caused by the strain-induced formation of martensite (α'). Additionally, the intensity of the α' -martensite diffraction peaks increased along with the strain amplitude.

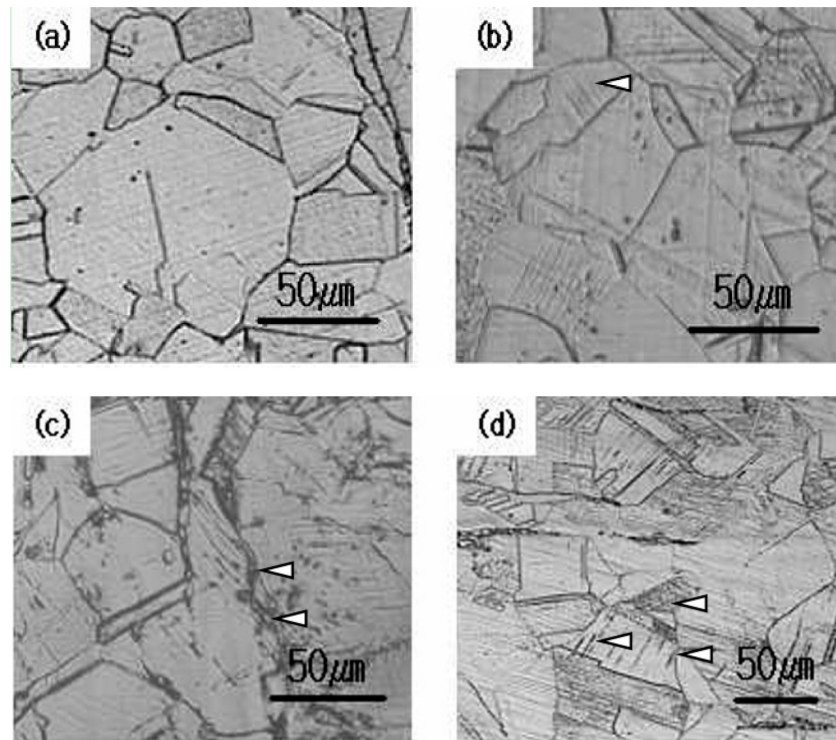


Figure 3. Optical micrographs showing α' -martensite in the specimens after low-cycle fatigue failure under various strain amplitudes: (a) as-received specimen; (b) 1.1% ($N_f = 578$); (c) 1.4% ($N_f = 342$); and (d) 1.7% ($N_f = 182$).

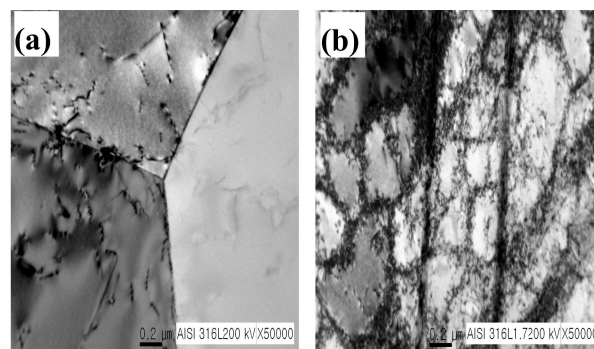


Figure 4. Transmission electron micrographs showing dislocation substructures in the specimens after low-cycle fatigue failure: (a) as-received specimen and (b) 1.7% ($N_f = 182$).

Figure 6 shows the changes in the magnetic properties of the fatigue-failed specimens as a function of the total strain amplitude. The magnetic coercivity, the saturation magnetization, and the remanence increased with an increasing strain amplitude. The monotonic increase of the magnetic parameters with the strain amplitude could be closely related to the presence of magnetic particles in austenitic AISI 316L stainless steels. However, as mentioned earlier, the austenite matrix is a non-ferromagnetic phase. Consequently, there must be another reason for the increase in the material's magnetic parameters.

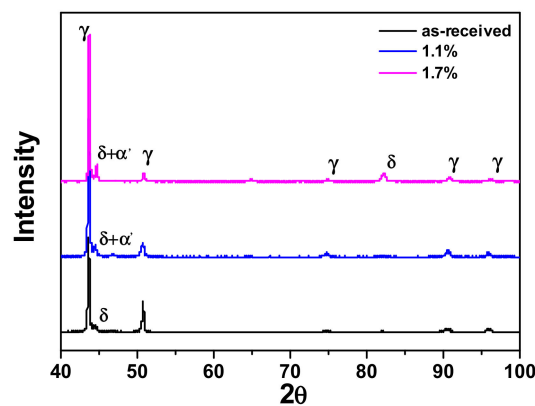


Figure 5. XRD profiles of the fatigue-failed specimens under various strain amplitudes. The intensity of the $\delta + \alpha'$ diffraction peak increased with the strain amplitude.

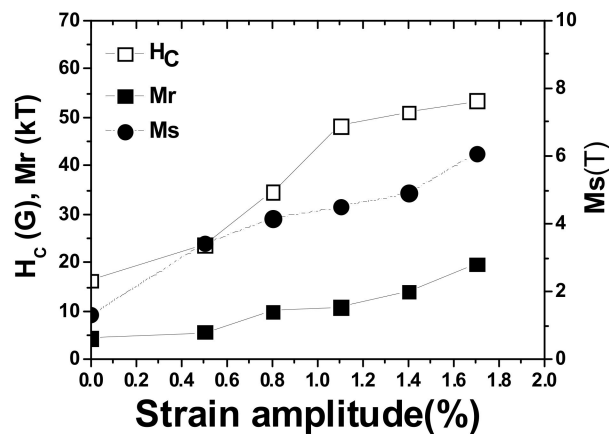


Figure 6. Change in the magnetic coercivity (H_c), saturation magnetization (M_s), and remanence (M_r) of the fatigue-failed specimens under various strain amplitudes.

The strain-induced martensite could have a reasonable influence on the magnetic properties of the specimen. The slip and twin boundaries could present an obstacle to the movement of the magnetic domain, resulting in an increase in the magnetic parameters [26]. In addition, dislocations may have a primary effect on the domain wall movement, and this would be another reasonable cause for variation in magnetic parameters. Principally, the strain-induced martensite had a reasonable influence on the increase of the material's magnetic properties because of its ferromagnetic property. The austenite phase is non-ferromagnetic, whereas α' -martensite is ferromagnetic. The magnetic parameters of the fatigued specimens consisting of austenite and α' -martensite can be correlated with the level of the strain-induced α' -martensite present in the specimens. The volume fraction of α' -martensite ($V_{\alpha'}$) was calculated using Equation (5) [27]:

$$V_{\alpha'} = \frac{(\sigma_s)}{(\sigma_s)_{f=1}} \quad (5)$$

In Equation (5), $(\sigma_s)_{f=1}$ is the specifically saturated magnetization for a purely martensitic state (i.e., $f = 1$), 143 emu/g, and (σ_s) is that of the fatigued specimen.

Figure 7 shows the volume fraction of α' -martensite as a function of the strain amplitude. It shows that there is a monotonic increase in the volume fraction of α' -martensite in austenitic AISI 316L stainless steel consistent with an increase in the strain amplitude. Both the ferrite scope and value stream mapping (VSM) technologies are based on variations in the magnetic properties of test materials.

According to this study, delta ferrite could be a primary microstructure before fatigue deformation, with magnetic characteristics. Additionally, after fatigue deformation, the α' -martensite must represent an important phase of the magnetic property exhibited by austenitic AISI 316L stainless steel. The fact that the volume fraction of the strain-induced martensite increases with an increased strain amplitude is a very reasonable result of the plastic deformation. The MFM image was generated by measuring the amplitude or phase change of the cantilever's oscillations, produced by the magnetic force between the structure's surface and the magnetized cantilever. MFM images contain information on magnetic domain distributions of a sample surface. Figure 8 shows MFM images of both the domain structures in the as-received specimens and of the specimens after subjection to a 1.7% strain amplitude. While the as-received specimen reveals no distinct domain structure, the specimen subjected to a 1.7% strain amplitude exhibits a clear domain structure caused by the strain-induced martensite formation resulting from fatigue deformation.

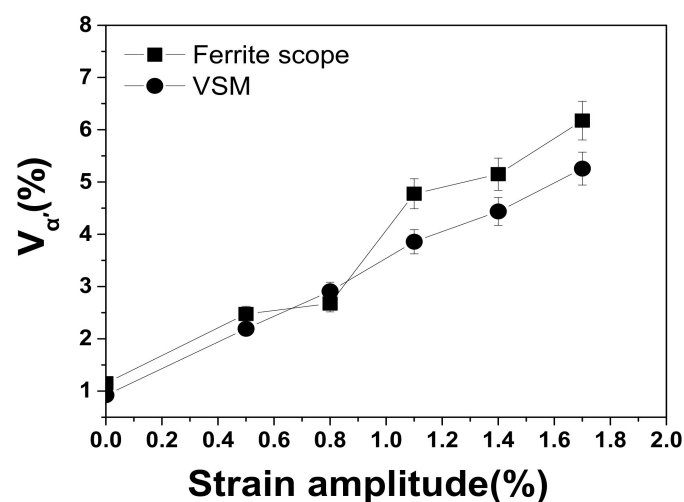


Figure 7. Variation in the volume fraction of α' -martensite measured by ferrite scope and VSM in fatigue-failed specimens after exposure of the material to various strain amplitudes. The volume fraction of α' -martensite increased linearly with the fatigue strain amplitude.

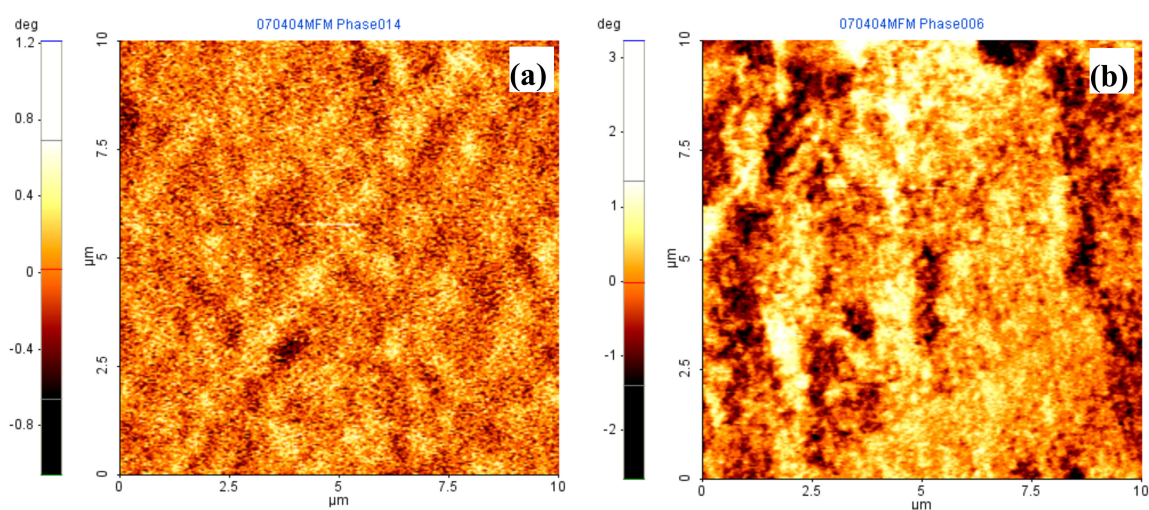


Figure 8. Magnetic force microscopy showing the specimens' domain substructure before and after low-cycle fatigue failure: (a) as-received specimen and (b) 1.7% ($N_f = 182$). There is no distinct domain structure in the as-received specimen, but the specimen subjected to 1.7% strain amplitude shows a clear domain structure.

In general, magnetic force microscopy was developed as a scanning probe technique for mapping magnetic field distributions in test materials on a microscopic scale. The color-contrast MFM images in Figure 8 show distinct, dark and bright stripes, indicating the presence of a magnetic domain structure. Because the MFM tip is magnetized downward, the bright stripe domains are magnetized in an upward direction, whereas the dark domains are magnetized in a downward direction [28].

Figure 9 shows the acoustic signal and the spectrum of the ultrasonic wave. In this test, a narrow-band 5-MHz transducer was used as a transmitter, and a wide-band 10-MHz transducer was used as a receiver. Because a narrow band signal is advantageous for effectively detecting higher harmonic amplitudes, a 5-MHz toneburst signal with a Hanning window was used to transmit the waveform. The length of the burst was 10 cycles, ensuring that both the fundamental frequency, as well as its double frequency for the second-order harmonic wave, were detected well.

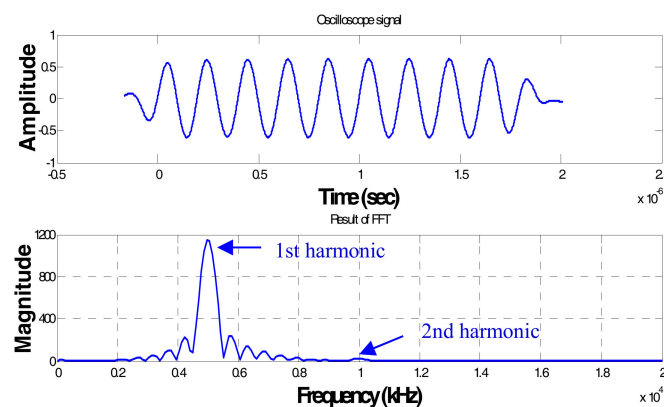


Figure 9. Ultrasonic signal wave and its spectral waveform for the specimen subjected to 1.7% strain amplitude. The signal-processed FFT waveform shows a weak second-order harmonic wave in addition to a strong first-order harmonic wave.

The second-order harmonic amplitude depends on the fundamental frequency amplitude, as shown by Equation (4). Based on the theoretical background, the second-order harmonic amplitude is linearly proportional to the square of the fundamental amplitude, as shown in Equation (1). This means that when the wave number and propagation distance are fixed, the parameter β' is constant regardless of the variation in the fundamental frequency amplitude. Figure 10 shows the relationship between A_1^2 and A_2 when the input signal amplitude is increased. The slope of the relationship between A_1 and A_2 is the nonlinearity parameter of the ultrasonic wave.

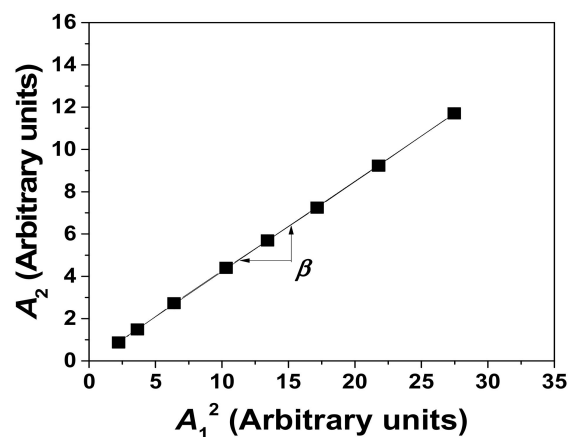


Figure 10. The relationship between A_1^2 and A_2 with various input signal amplitudes, showing a good linear relationship. The slope of this linear relationship is the nonlinearity parameter (β).

The measurement was made ten times under the same conditions. The results show a linearly proportional relationship and consistency with the above theoretical expectation. Figure 11 depicts the variation in the acoustic nonlinearity of AISI 316L stainless steel fatigue-failed specimens under various strain amplitudes. The acoustic nonlinearity increased with strain amplitude due to the occurrence of fatigue-driven plastic deformation, and is therefore closely related to the strain amplitude and to the accumulation of fatigue deformation [29]. To understand the microstructural features that influence the distortion of the acoustic wave and result in superharmonic generation, we refer to the previously shown and discussed microstructural evolution during fatigue damage.

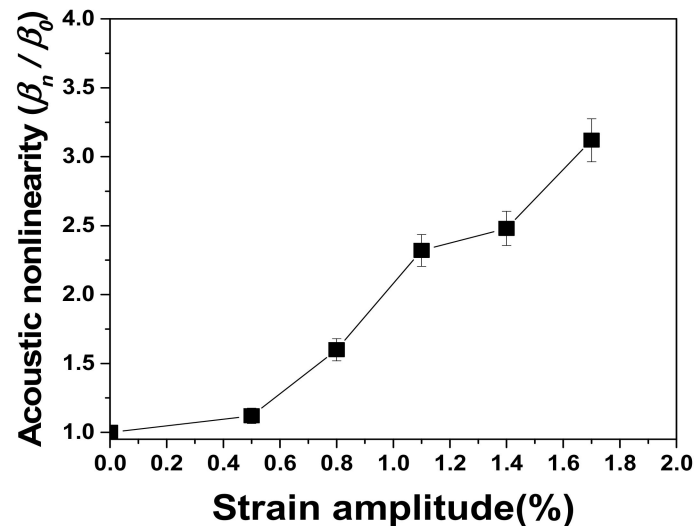


Figure 11. Variation in the acoustic nonlinearity of AISI 316L stainless steel fatigue-failed specimens under various strain amplitudes. β_0 is the nonlinearity parameter of the as-received specimen, and β_n is the nonlinearity parameter of the fatigue-failed specimen.

Many authors have discussed and explained that dislocations that occur during fatigue play an important role in generating ultrasonic wave super-harmonics. Suzuki et al. [10] explains that the acoustic nonlinearity parameter is related to the dislocation loop length (L), the dislocation density (Δ), and the stress (σ), by using the following equation [30]:

$$\beta \propto \Delta L^4 \sigma \quad (6)$$

Equation (6) shows that β is linearly dependent on the stress and the dislocation density. Here, we considered the effects of both parameter strain and microstructural changes during fatigue when discussing the variation of the acoustic nonlinearity parameter in relation to the strain amplitude. Figure 4 shows that the TEM microstructure exhibited increased dislocation densities, while we also observed clear dislocation cell structures. The cell interior was dislocation-free and corresponded to fatigue strain softening. Martensite, located in steel crystal areas, is a distorted body-centered cubic (BCC) ferrite lattice that still contains dissolved carbon and is full of defects. There is far more atomically dissolved carbon in the martensite than would be acceptable for stable ferrite, and this dissolved carbon distorts the lattice. This lattice distortion could be the primary reason for the wave distortion that occurs when the ultrasonic wave propagates through the test materials. From this wave distortion, super-harmonics may be generated due to the nucleation of strain-induced martensite, which strongly depends on the strain amplitude.

The dependence of the magnetic coercivity and the acoustic nonlinearity on the volume fraction of α' -martensite shows a good linear relationship with a high R-squared value, as shown in Figure 12. We note that, because of the NDE technique's availability, the coercivity and the acoustic nonlinearity

parameter could be successfully used to characterize α' -martensite during the fatigue deformation of austenitic stainless steel. Consequently, both the coercivity parameter and the acoustic nonlinearity parameter offer a potential approach for evaluating the fatigue-mediated damage of austenitic AISI 316L stainless steel.

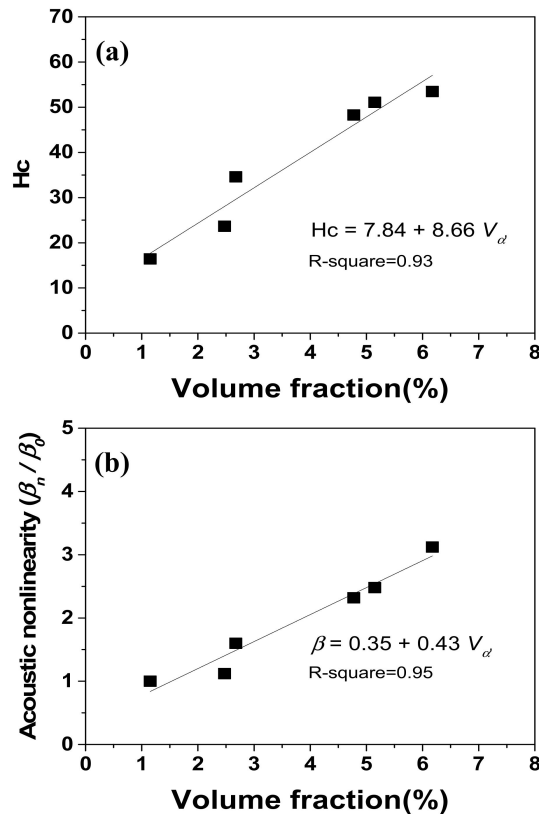


Figure 12. A linear relationship between acoustic nonlinearity and magnetic coercivity as a function of the volume fraction of α' -martensite: (a) magnetic coercivity and (b) acoustic nonlinearity.

4. Conclusions

The strain-induced formation of α' -martensite during the low-cycle fatigue deformation of austenitic AISI 316L stainless steel was investigated using magnetic and acoustic nondestructive evaluation techniques. Cyclic hardening was observed within several tens of cycles and then followed by slight second hardening at strain amplitudes ranging from 0.8% to 1.1%. The test materials exhibited strain hardening without reaching their saturated value until the final fracture occurred at strain amplitudes over 1.1%. The initial cyclic hardening was attributed to an increased dislocation density, and the subsequent secondary hardening was ascribed to the presence of α' -martensite induced by fatigue. The volume fraction of strain-induced α' -martensite increased with an increasing cyclic strain amplitude, measured quantitatively by saturation magnetization, ferrite scope. The increase in α' -martensite was also evaluated by means of an ultrasonic nonlinearity parameter measured via an oblique incidence technique. We posit that the α' -martensite may distort the matrix lattice in austenitic stainless steel, resulting in the distortion of ultrasonic waves. Super-harmonics were generated by nucleation of the strain-induced martensite, and this generation was itself strongly dependent on the strain amplitude. Consequently, we observed a good linear relationship between acoustic nonlinearity and the volume fraction of α' -martensite. This study suggests that the fatigue life of austenitic AISI 31 can be predicted by monitoring the α' -martensite transformation during fatigue using magnetic coercivity and acoustic nonlinearity measurements.

Acknowledgments: This research was supported by Basic Science Research Program through the National Research Foundation of Korea (NRF) funded by the Ministry of Education (2017R1D1A3B03028681) and MSIP (No. 2008-0062283).

Conflicts of Interest: The author declares no conflict of interest.

References

1. Song, M.; Gurao, N.P.; Qin, W.; Szpunar, J.A.; Guan, K.S. Deciphering deviation in mechanical properties of differently processed AISI 316L austenitic stainless steel using the small punch test. *Mater. Sci. Eng. A* **2015**, *628*, 116–123. [[CrossRef](#)]
2. Hsu, J.-P.; Wang, D.; Kahn, H.; Ernst, F.; Michal, G.M.; Heuer, A.H. Fatigue crack growth in interstitially hardened AISI 316L stainless steel. *Int. J. Fatigue* **2013**, *47*, 100–105. [[CrossRef](#)]
3. Akbarimousavi, S.A.A.; GohariKia, M. Investigations on the mechanical properties and microstructure of dissimilar cp-titanium and AISI 316L austenitic stainless steel continuous friction welds. *Mater. Des.* **2011**, *32*, 3066–3075. [[CrossRef](#)]
4. Petráš, R.; Škorík, V.; Polák, J. Thermomechanical fatigue and damage mechanisms in Sanicro 25 steel. *Mater. Sci. Eng. A* **2016**, *5*, 52–62. [[CrossRef](#)]
5. Ziemian, C.W.; Ziemian, R.D.; Haile, K.V. Characterization of stiffness degradation caused by fatigue damage of additive manufactured parts. *Mater. Des.* **2016**, *109*, 209–218. [[CrossRef](#)]
6. Das, A.; Tarafder, S.; Chakraborti, P.C. Estimation of deformation induced martensite in austenitic stainless steels. *Mater. Sci. Eng. A* **2011**, *529*, 9–20. [[CrossRef](#)]
7. Leber, H.J.; Niffenegger, M.; Tirbonod, B. Microstructural aspects of low cycle fatigued austenitic stainless tube and pipe steels. *Mater. Charact.* **2007**, *58*, 1006–1015. [[CrossRef](#)]
8. Kim, C.S. Creep characterization in advanced heat-resistance steel using ultrasonic nonlinearity. *Mater. Trans.* **2012**, *53*, 2028–2033. [[CrossRef](#)]
9. Filho, I.R.; Sandim, M.J.R.; Cohen, R.; Nagamine, L.C.C.M.; Hoffmann, J.; Bolmaro, R.E.; Sandim, H.R.Z. Effects of strain-induced martensite and its reversion on the magnetic properties of AISI 201 austenitic stainless steel. *J. Magn. Magn. Mater.* **2016**, *419*, 156–165. [[CrossRef](#)]
10. Snizhnoi, G.V.; Rashedchupkyna, M.S. Magnetic State of Deformed Austenite before and after Martensite Nucleation in Austenitic Stainless Steels. *J. Iron Steel Res. Int.* **2012**, *19*, 42–46. [[CrossRef](#)]
11. Ryu, K.S.; Kim, C.S.; Baek, U.B.; Lee, J.S. Nondestructive evaluation for remanent life of aged 12Cr ferrite heat resisting steel by reversible permeability. *J. Magn. Magn. Mater.* **2013**, *326*, 257–260. [[CrossRef](#)]
12. Ryu, K.S.; Park, J.S.; Nahm, S.H.; Yu, K.M.; Kim, Y.B.; Son, D. Nondestructive evaluation of aged 1Cr–1Mo–0.25 V steel by harmonic analysis of induced voltage. *J. Magn. Magn. Mater.* **2001**, *231*, 294–298.
13. Kim, C.S. Characterization of reversible permeability in USC steel during thermal aging. *Phys. Status Solidi A* **2010**, *207*, 97–100. [[CrossRef](#)]
14. Kim, C.S.; Jhang, K.Y. Fatigue-induced microdamage characterization of stainless steel 316L using innovative nonlinear acoustics. *Chin. Phys. Lett.* **2012**, *29*, 060702. [[CrossRef](#)]
15. Li, W.; Cui, H.; Wen, W.; Su, X.; Engler, C.C. In situ nonlinear ultrasonic for very high cycle fatigue damage characterization of a cast aluminum alloy. *Mater. Sci. Eng. A* **2015**, *645*, 248–254. [[CrossRef](#)]
16. Saga, S.P.; Metya, A.K.; Ghosh, M.; Sivaprasad, S. Effect of microstructure on non-linear behavior of ultrasound during low cycle fatigue of pearlitic steels. *Mater. Sci. Eng. A* **2011**, *528*, 2895–2898.
17. Walker, S.V.; Kim, J.Y.; Qu, J.; Jacobs, L.J. Fatigue damage evaluation in A36 steel using nonlinear Rayleigh surface waves. *NDT E Int.* **2012**, *48*, 10–15. [[CrossRef](#)]
18. Drewry, M.A.; Wilcox, P.D. One-dimensional time-domain finite-element modeling of nonlinear wave propagation for non-destructive evaluation. *NDT E Int.* **2014**, *61*, 45–52. [[CrossRef](#)]
19. Fierro, G.P.M.; Calla, D.; Ginzburg, D.; Ciampa, F.; Meo, M. Nonlinear ultrasonic stimulated thermography for damage assessment in isotropic fatigued structures. *J. Sound Vib.* **2017**, *404*, 102–115. [[CrossRef](#)]
20. Aleksić, V.; Milović, L.J.; Aleksić, B.; Hemer, A.M. Indicators of HSLA steel behavior under low cycle fatigue loading. *Procedia Struct. Integr.* **2016**, *2*, 3313–3321. [[CrossRef](#)]
21. Vine, K.; Cawley, P.; Kinloch, A.J. Comparison of normal and oblique incidence ultrasonic measurements for the detection of environmental degradation of adhesive joints. *NDT E Int.* **2002**, *35*, 241–253. [[CrossRef](#)]

22. Viswanath, A.; Rao, B.P.C.; Mahadevan, S.; Parameswaran, P.; Jayakumar, T.; Raj, B. Nondestructive assessment of tensile properties of cold worked AISI type 304 stainless steel using nonlinear ultrasonic technique. *J. Mater. Process. Technol.* **2011**, *211*, 538–544. [[CrossRef](#)]
23. Ren, G.; Kim, J.B.; Jhang, K.Y. Relationship between second- and third-order acoustic nonlinear parameters in relative measurement. *Ultrasonics* **2015**, *56*, 539–544. [[CrossRef](#)] [[PubMed](#)]
24. Kollerov, M.; Lukina, E.; Gusev, D.; Mason, P.; Wagstaff, P. Impact of material structure on the fatigue behavior of NiTi leading to a modified Coffin–Manson equation. *Mater. Sci. Eng. A* **2013**, *585*, 356–362. [[CrossRef](#)]
25. Roy, S.C.; Goyal, S.; Sandhya, R.; Ray, S.K. Low cycle fatigue life prediction of 316 L(N) stainless steel based on cyclic elasto-plastic response. *Nucl. Eng. Des.* **2012**, *253*, 219–225. [[CrossRef](#)]
26. Ma, B.; Li, C.; Han, Y.; Wang, J. $\gamma \rightarrow \alpha'$ Martensitic transformation and magnetic property of cold rolled Fe-20Mn-4Al-0.3C steel. *J. Magn. Magn. Mater.* **2016**, *419*, 249–254. [[CrossRef](#)]
27. Botshekan, M.; Degallaix, S.; Desplanques, Y.; Polak, J. Tensile and LCF properties of AISI 316LN SS at 300 and 77 K. *Fatigue Fract. Eng. Mater. Struct.* **1998**, *21*, 651–660. [[CrossRef](#)]
28. Öztürk, O.; Fidan, M.; Mändl, S. MFM imaging of expanded austenite formed on 304 SS and CoCrMo alloys. *Surf. Coat. Technol.* **2014**, *256*, 15–22. [[CrossRef](#)]
29. Su, Z.; Zhou, C.; Hong, M.; Cheng, L.; Wang, Q.; Qing, X. Acousto-ultrasonics-based fatigue damage characterization: Linear versus nonlinear signal features. *Mech. Syst. Signal Process.* **2014**, *45*, 225–239. [[CrossRef](#)]
30. Cai, Y.Q.; Sun, J.Z.; Liu, C.J.; Ma, S.W.; Wei, X.C. Relationship between Dislocation Density in P91 Steel and Its Nonlinear Ultrasonic Parameter. *J. Iron Steel Res. Int.* **2015**, *22*, 1024–1030. [[CrossRef](#)]



© 2017 by the author. Licensee MDPI, Basel, Switzerland. This article is an open access article distributed under the terms and conditions of the Creative Commons Attribution (CC BY) license (<http://creativecommons.org/licenses/by/4.0/>).